# Highlights

## Co-optimization of fuel properties, combustion system geometry, and injection strategy for conventional diesel fuel

Flavio D.F. Chuahy, Marco Delchini, Corey Trobaugh, Jeff Klopfenstein, Tim Shipp

- Changes in physical properties did not have a significant impact on engine efficiency.
- Fuel density was the only parameter to show any interaction with input parameters.
- Physical properties cannot be leveraged in a co-optimization context to obtain significant efficiency benefits.

# Co-optimization of fuel properties, combustion system geometry, and injection strategy for conventional diesel fuel

Flavio D.F. Chuahy[a], Marco Delchini[a], Corey Trobaugh[b], Jeff Klopfenstein[b] and Tim Shipp[b]

[a]Oak Ridge National Laboratory, 1 Bethel Valley Road, Oak Ridge, Tennessee, 37830, USA
[b]Cummins Inc., 1900 McKinley Avenue, Columbus, Indiana, 47201, USA

ARTICLE INFO

*Keywords*:
co-optimization
high efficiency
combustion
fuel properties
machine learning

ABSTRACT

Studies have shown that fuel properties can impact an engine's operation in several ways, including ignition delay, sooting tendency, mixture formation, and combustion temperature. In mixing-controlled compression ignition (MCCI) engines, the fuel system design and piston bowl geometry significantly affect combustion performance and emissions. Based on current information, it is difficult to draw conclusions about fuel property effects and sensitivities. The central fuel hypothesis approach used in the US Department of Energy Co-Optima program has worked well for spark ignition fuels: identifying critical fuel property ranges is sufficient to screen fuel blends that are expected to maximize efficiency and reduce pollutant emissions. However, for MCCI-relevant fuels, the information gained from past studies is not sufficient to build such a merit function or to allow for performing a similar screening of fuel blends. It is hypothesized that a co-optimization of a fuel's physical and chemical properties, combustion system geometry, and injection strategy could leverage synergies between the effects of the fuel properties and geometries, resulting in improved performance over state-of-the-art. A machine learning–assisted unconstrained global optimization algorithm was used to explore a design space comprising 23 independent variables. The results show that physical property effects were minimal even for large variations in fuel properties, and the only interaction effect that was observed was the effect of varied fuel density parameters on fuel/air mixture formation. Nevertheless, these interactions were not sufficient in magnitude to significantly affect optimization results. Therefore, analysis of the results suggests that fuel physical properties cannot be leveraged in a co-optimization context to increase engine efficiency.

setspace

## 1. Introduction

The US Department of Energy Co-optimization of Fuels and Engines (Co-Optima) program set out to examine fuels as design variables that can be optimized in combination with engine geometry and injection strategy to significantly improve the state of the art. The concept of co-optimizing fuel properties and engines led to the idea of a central fuel hypothesis stating that the physical and chemical properties of fuel—including density, octane/cetane number, heat of vaporization, and so on—are sufficient to define fuel performance, irrespective of their chemical class composition



*Corresponding author
dalfornochuf@ornl.gov (F.D.F. Chuahy)
https://www.ornl.gov/staff-profile/flavio-dal-forno-chuahy (F.D.F. Chuahy)
ORCID(s):

(e.g., alkanes, aromatics, olefins). Therefore, under this hypothesis, identifying critical fuel property ranges is sufficient to screen the fuel blends that are expected to maximize efficiency and reduce pollutant emissions. This approach has worked well for spark ignition fuels. However, for mixing-controlled compression ignition (MCCI)-relevant fuels, the information gained from past studies is not sufficient to build that understanding and to perform a similar screening of fuel blends.

The study of fuel property effects in MCCI engines has been of interest for decades. Previous investigations by Groendyk and Rothamer [1], Chuahy and Kokjohn [2], Ra et al. [3], Zhang et al. [4], and Liu et al. [5] have shown that the effects of physical properties are secondary to the effects of chemistry. All studies showed some limitations, such as minimal physical property variations that did not allow general conclusions to be drawn regarding fuel property effects [4]. To address that limitation, recent work [6] expanded these studies and explored the impact of physical properties more broadly by computationally isolating physical properties and exploring extreme physical property changes. The results of that study showed that, as in all previous studies, changes in fuel physical properties alone are insufficient to significantly change the efficiency vs. emissions trade-off and achieve better performance. These changes include either changing the distillation curve [6] or manipulating the injection strategy [7]. Several studies have shown that changes in diesel chemical properties have a significant impact on performance and engine emissions. Icingur and Altiparmak [8] show emissions benefits when the fuel's cetane number is increased in a diesel engine. Ullman et al. [9] experimentally studied the impact of changes in the cetane number, also finding emissions benefits resulting from an increased value. Yuan et al. [10] also show how changing the cetane number affects diesel engine combustion. They concluded that a lower cetane number was more advantageous because of a higher potential for premixing of the fuel, derived from its lower chemical reactivity. However, the study only includes a single-injection strategy; no significant parametric investigation was conducted from which general conclusions could be drawn about the performance effects of changing the cetane number. In summary, the studies show that physical properties alone do not have a significant impact on the combustion performance of MCCI engines, but the cetane number does and can be leveraged for improved efficiency and emissions trade-offs. Nevertheless, none of the studies attempt to leverage the engine's architectural or injection strategy modifications to investigate potential synergies between the fuel properties and the engine.

The combustion system geometry (piston bowl geometry, cylinder head geometry, injector configuration, etc.) has evolved over 100 years and has traditionally been a critical design focus for compression ignition engines. A number of studies have focused on leveraging optimization algorithms and geometry paramaterizations to optimize the geometry of the MCCI combustion chamber. Generally, two types of studies have been conducted. In the first type, different piston geometries are predefined, and experiments or simulations are conducted to explore the benefits of each geometry. Busch et al. [11] showed that results from studies using computational fluid dynamics (CFD) demonstrate performance improvements and show the effects of piston design shapes on efficiency and emissions results. However,

these studies provide limited information on the interactions between parameters to be quantified. The second type of study employs CFD and leverages optimization techniques such as evolutionary algorithms to explore a design space more comprehensively [12–16]. Some limitations with the second type of study include the following simplifications:
(1) the use of sector meshes [11, 12, 17, 18] to save computational time, which eliminates the effects of plume-to-plume interaction and flow swirl,
(2) the use of simplified chemical representations for diesel fuel with a single or few components that do not match its chemical and physical properties [11–13, 16–18],
(3) simplified parameterization of the fuel bowl with only 2–4 variables, not allowing for analysis beyond the preconceived baseline shape [11, 13, 17, 19],
(4) simplifications of the NOx formation mechanism to a two-step model and soot mechanisms to simple air–fuel ratio–based models that have been shown not to be trend-wise correct [12, 16, 18], and
(5) investigation of piston geometries in isolation, with injector geometry or injection strategy variations only performed on optimal results, or not investigated at all [13, 14, 18].
Nevertheless, these studies have demonstrated the usefulness of optimization algorithms in exploring complex parametric effects emerging from the interaction of multiple physical processes inside a combustion chamber. Although they serve their purpose in optimizing control parameters for specific engines and conditions relevant to this work, general conclusions about the nature of interactions are often difficult to extract. Finally, because none of the mentioned works coupled chemical and physical properties variations to the optimization process, their interaction potential with engine geometry and injection strategy is unknown.

Based on this review of published works, it is clear that physical property effects have been shown to be insignificant in the context of MCCI. However, these fuel effects have not been studied in concert with other variations to explore the potential synergies. Therefore, it is hypothesized that a co-optimization of fuel physical and chemical properties, combustion system geometry, and injection strategy can achieve improvements over the state-of-the-art by finding parameter interactions that can be leveraged for improved performance. Based on that hypothesis, the work presented herein used a machine learning–assisted global optimization algorithm available in DAKOTA [20] to explore co-optimization of fuel physical properties and engine geometry for a fixed fuel chemical composition. A wide design space comprising 23 independent variables that include 7 fuel physical properties, 3 fuel system geometry parameters, 6 bowl geometry parameters, and 7 injection strategy related parameters was defined and used in the optimization. The computational model developed was designed to avoid the typical model simplifications traditionally used to save computational time. The model included comprehensive chemical reaction mechanisms for diesel fuel, NOx, and polycyclic aromatic hydrocarbons (PAHs) for soot predictions. Additionally, the CFD model was constructed as a full 360-degree geometry initialized with velocity and temperature profiles obtained by performing the complete intake,

combustion, and exhaust processes multiple times in sequence, thus providing a more accurate initial condition at intake valve closing (IVC). The goal of this work is not to find a single optimal condition like in an engineering design problem. The goal of this work is to generate reliable data that is at the Pareto front of optimal solutions to study the potential for co-optimization of fuel properties and engine geometry simultaneously.

The high-performance computing (HPC) resources of the Compute Data Environment for Science (CADES) at Oak Ridge National Laboratory (ORNL) were leveraged to accomplish this work. To the best of the authors' knowledge, this is the only analysis that includes fuel property variations along with geometry and injection strategy parameters. The objectives of this work were (1) to quantify the interaction effect of physical properties with all geometry and injection strategy parameters, (2) to optimize the piston geometry, injection strategy, injection system geometry, and fuel physical properties for conventional diesel fuel, and (3) to demonstrate control parameter interactions to identify synergies, if existent, that can be leveraged in a co-optimization context.

## 2. Methodology

### 2.1. Computational Setup

3D CFD simulations were performed using CONVERGE 3.0.24 to explore the optimization design space. An open cycle model was developed to simulate the air intake, exhaust, and combustion processes. The engine geometry represents a single cylinder of a Cummins ISB engine. The engine baseline geometry and injector configuration are shown in Table 1. The engine and injector geometries were scanned and recreated for CFD. More details about the computational geometry are shown in Chuahy et al. [6]. Table 2 summarizes the computational setup. The settings used in a previous grid independence study [6] were applied to this analysis. The fuel spray was simulated with a Lagrangian blob approach. Spray break-up was modeled with the Kelvin-Helmholtz Rayleigh-Taylor (KH-RT) approach [21]. Droplet collision, drag, and evaporation were modeled using the No Time Counter (NTC) [22], dynamic [23], and Frossling correlation [24] approaches, respectively. A 4 mm base cell size was used in the intake and exhaust regions, with a 1 mm base cell size in the in-cylinder region. Adaptive mesh refinement (AMR) with a minimum cell size of 0.25 mm was used in all regions based on velocity and temperature gradients. Although the fuel chemical surrogate was represented by multiple species, as discussed below, multi-component evaporation was not considered. A single species was used for the physical property representation to facilitate the parametric variation of each property. All fuel physical properties were defined to best represent conventional diesel fuel. Combustion was solved through direct chemistry integration using a well-stirred reactor assumption coupled with an adaptive zoning scheme. Temperature and equivalence ratio binning were used to reduce chemistry integration time. A comprehensive diesel chemical mechanism was used to accurately represent the fuel chemistry. The mechanism includes 319 species and 1,797 reactions, including thermal and prompt NOx mechanisms and PAH chemistry for soot modeling. Soot emissions were

**Table 1**
Baseline engine and injector geometry.

| | |
|---|---|
| Bore [mm] | 107 |
| Stroke [mm] | 124 |
| Connecting rod length [mm] | 192 |
| Baseline compression ratio [-] | 20 |
| Injector included angle [o] | 145 |
| Injector nozzle size [$\mu$m] | 141 |
| Number of nozzle holes [-] | 8 |

**Table 2**
CFD sub-model and grid setup.

| | |
|---|---|
| CFD software | CONVERGE 3.0.24 |
| Fuel injection | Blob |
| Droplet breakup | KH–RT |
| Droplet collision | NTC |
| Droplet drag | Dynamic |
| Droplet evaporation | Frossling |
| Droplet wall interaction | Film |
| Film splash | O'Rourke |
| Combustion | Direct chemistry integration |
| Turbulence | RANS RNG k-$\epsilon$ |
| Base mesh size | 1 mm |
| Adaptive mesh refinement cell size based on temperature and velocity | 0.25 mm |
| NOx emissions | Prompt and thermal NOx mechanisms |
| Soot emissions | Particlate mimic detailed soot model |

modeled using a particulate mimic detailed soot model available in CONVERGE. Turbulence was modeled using a conventional Reynolds-averaged Navier-Stokes (RANS) RNG-k epsilon approach.

## 2.2. Fuel Surrogate

A surrogate formulation for conventional diesel fuel was developed to match the derived cetane number, density, hydrogen-to-carbon ratio, and fuel distillation curve. Table 3 shows the fuel surrogate composition and compares important properties of measured vs. surrogate values. The pallet of species for surrogate optimization was chosen based on availability in the chemical mechanism. Five species were found to be sufficient to achieve a good match between surrogate and fuel properties. The surrogate was used in the simulations to represent the chemistry of the fuel. To facilitate interpretation of variations in each physical property, multi-component evaporation was not considered. Therefore, the surrogate fuel was represented by a composite using the physical properties of conventional diesel fuel available in CONVERGE.

## 2.3. Optimization Operating Condition

The operating condition of the engine used for the optimization was chosen based on the availability of engine steady-state data and analysis of relevant California Air Resources Board (CARB) certification duty-cycles. Figure

**Table 3**
Conventional diesel fuel surrogate and fuel properties.

| | |
|---|---|
| a-methylnaphthalene [%] | 12.91 |
| n-dodecane [%] | 14.88 |
| decalin [%] | 53.85 |
| iso-cetane [%] | 11.41 |
| n-octadecane [%] | 6.95 |
| Cetane number (ASTM D613) [–] | 45.3 |
| Derived cetane number (surrogate) [–] | 45.4 |
| Lower heating value (ASTM D240) [MJ/kg] | 43.19 |
| Lower heating value (surrogate) [MJ/kg] | 42.8 |
| Density (ASTM D4052) [kg/m$^3$] | 827.0 |
| Density (surrogate) [kg/m$^3$] | 840.0 |
| Surface Tension [mN/m] | 25.8 |
| Dynamic Viscosity [cPoise] | 9.8 |
| Bulk Modulus [bar] | 22700 |

1 shows the Greenhouse gas emissions model (GEM) CARB and the transient CARB certification cycles as bubble plots. A larger bubble indicates a longer amount of time spent in that region of the engine speed vs. the torque map. This information can be used to determine the conditions that, if optimized, can achieve the greatest proportional improvements in cycle performance. The condition chosen for the optimization is shown in Figure 1 with an engine speed of 1600 rpm and a torque of 544 N–m. The condition was chosen based on the availability of steady-state engine data that could be used for validation. Although the chosen speed is lower than those seen in the GEM CARB cycle, the load is appropriate. Given the data points available in this version of the Cummins ISB engine, the authors decided that optimizing the combustion system at a relevant load was more important than matching the engine speed, which is only 200 rpm lower than the most utilized engine speed range in the GEM CARB cycle.

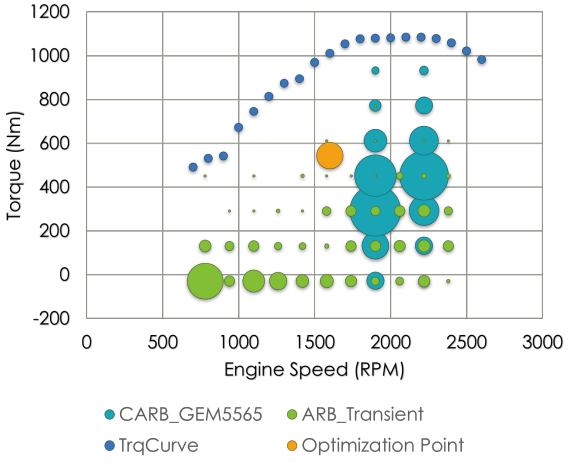


**Figure 1:** Engine speed as a function of engine torque displaying the engine torque curve and two certification duty-cycles as bubble plots. Operating condition chosen for optimization is shown.

**Table 4**
Experimental condition chosen for model validation and optimization.

| | |
|---|---|
| Engine speed [rpm] | 1600 |
| Engine torque [N–m] | 544 |
| Fuel | Conventional diesel |
| Exhaust gas recirculation (EGR) [%] | 16.5 |
| Intake Pressure [kPa] | 165 |
| Fuel mass [kg/cycle] | 6.292e-5 |
| Injection pressure [bar] | 1500 |
| Pre-injection timing [°aTDCf] | -11.9 |
| Main-injection timing [°aTDCf] | 0.0 |
| Post-injection timing [°aTDCf] | 17.2 |
| Pre-injection fraction [-] | 0.03 |
| Main-injection fraction [-] | 0.85 |
| Post-injection fraction [-] | 0.12 |

Table 4 shows the details of the chosen operating condition. The condition chosen employs a three-injection strategy, including a pilot-injection with 3% of the total fuel mass at -11.9° after top-dead-center of firing (aTDCf), a main injection with 85% of the total fuel mass at 0.0°aTDCf, and a post injection with 12% of the total fuel at 17.2°aTDCf at 1500 bar injection pressure. The condition also uses 16.5% of exhaust gas recirculation (EGR).

## 2.4. Model Validation

The model used in this work has been previously validated under various conditions with results show in [25, 26]. However, the model was further validated against the operating condition chosen for the optimization as the baseline, with conditions presented in Table 4. Figure 2 compares in-cylinder pressure and apparent heat release rate (AHRR) between experimental and simulation results. The results show that the model is capable of accurately capturing the timing of the premixed AHRR associated with the pilot injection, the main heat release event, and the third peak associated with post-injection combustion. The magnitude of the premixed spike is slightly underpredicted. Table 5 shows the comparison of NOx and soot emissions between experiments and simulation results. The model achieved excellent accuracy, with NOx emissions showing a discrepancy of 6%, and soot emissions showing a discrepancy of 18%, which is on par with the accuracy observed in the literature. The detailed prompt, thermal NOx chemical mechanism, and detailed particle mimic soot model are expected to provide significantly more accurate results in response to parametric changes than results obtained using the 2-step Zeldovich approximation for NOx or the Hiroyasu air-fuel ratio–based soot model [27, 28] typically used in the literature. Calculation of AHRR, efficiency and combustion efficiency used standard methodologies used in the literature and specific equations can be found in [29]. More information about the experimental setup and equipment utilized can be found in [26]

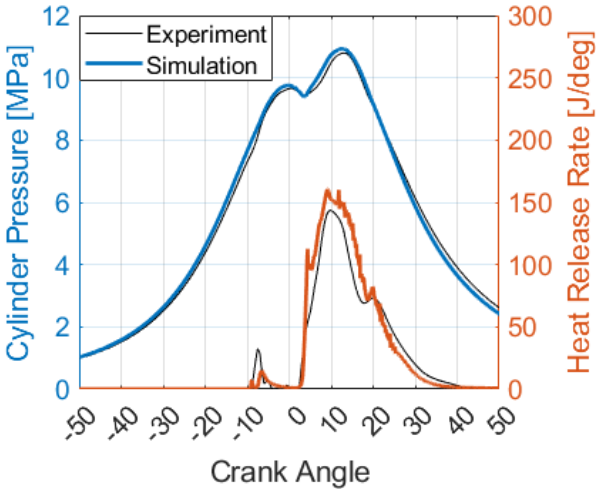


**Figure 2:** Comparison of experimental and simulated in-cylinder pressure and apparent heat release rate.

**Table 5**
Comparison of experimental and simulated NOx and soot emissions.

| Parameter | Experiments | Simulation |
|---|---|---|
| NOx emissions normalized [-] | 1.0 | 1.06 |
| Soot emissions normalized [-] | 1.0 | 0.82 |

## 2.5. Optimization Methodology and Approach

Figure 3 shows a schematic of the optimization workflow. The co-optimization required several software packages to be integrated. The Nuclear Energy Advanced Modeling and Simulation (NEAMS) workbench [30, 31], an analysis sequence processor and workflow management tool, was used to control the entire optimization process by facilitating a connection between DAKOTA and CAESES. The developed and validated 3D CFD model was provided for the optimization workflow via CAESES. CAESES is a specialized software package that allows easy parameterization of computer-aided design (CAD) geometries for optimization. CAESES also contains tools for process automation that were critical for integration of the workflow. DAKOTA, [20] a suite of iterative mathematical and statistical methods, was chosen for this optimization, and CONVERGE was used to perform the combustion simulations, as shown above.

The workflow was designed so that DAKOTA, the optimization algorithm, could feed conditions for evaluation to CAESES. CAESES then adjusted the CFD input files and geometry accordingly, submitted each individual simulation to the HPC cluster, and monitored simulation progress. Once each simulation was completed, CAESES was set up to extract important metrics from the simulation outputs (e.g., emissions index, efficiency, mechanical constraints). When all simulations in a batch were completed, the NEAMS workbench translated the outputs collected by CAESES into a format readable by DAKOTA. Using the resulting information, DAKOTA could then determine the next batch of simulations. The optimization was performed until no further improvement in efficiency was observed or expected.

DAKOTA offers a range of design exploration tools. The efficient global optimization (EGO) algorithm was chosen for this work as opposed to local or evolutionary search methods because of the large number of variables involved. These alternative algorithms are known to take too long to converge in the case of evolutionary algorithms [32], or they are often stuck in local minima based on initial search conditions, as in the case of local search methods. The EGO algorithm was developed to perform the unconstrained minimization of expensive implicit response functions such as the response function associated with engine efficiency. The method uses machine learning assistance through Gaussian process regression (GPR) models. The method builds an initial GPR global surrogate based on an initial sampling of points. In this work, 300 initial points were used. Assisted by the GPR surrogate, the algorithm then intelligently selects the additional samples that are expected to improve the current best solution. Within each iteration, the algorithm chooses points at which a formulated expected improvement function (EIF) is maximized. After each iteration is completed, the new data are used to update the GPR response surface and EIF so that new samples can be selected.

The optimization was designed to minimize the negative of the engine's gross indicated efficiency (GIE): to maximize GIE. At each iteration of the workflow, DAKOTA was asked to choose 20 new sampling points, 16 of which were chosen based on maximization of the EIF, and 4 of which were chosen at random to further reduce the chances of convergence to a local minimum. One challenge of an optimization workflow is to determine what value to assign to an unfeasible design. Unfeasible designs can be piston geometries that violate some constraints, or they can be certain designs that lead to a simulation crashing. Most unfeasible designs can be avoided by intelligently selecting the ranges for each independent variable. However, not all can be avoided. Because of the nature of the optimization method, the value assigned to an unfeasible design will be part of the GPR surrogate model which will affect its shape and the EIF, so care must be taken. The approach chosen for this work is that of the "constant liar" heuristic. The constant liar heuristic is a terminology adopted from the works of Ginsbourger et al. [33, 34] in which a larger value of the "lie" would result in a more exploratory optimization, and a lower value would result in a more exploitative optimization. Here, each unfeasible design is assigned a value of -30 % to balance the exploratory and exploitative nature of the optimization.

Figure 4 shows the parameterization used for the piston geometry. The bowl shape was parameterized with 10 different independent variables. The parameterization was chosen to allow step-lipped, re-entrant, and open bowl designs such that the shape could be fully defined by the optimization process and not by engineering intuition. Six parameters were chosen for the optimization in addition to the compression ratio. To adjust the compression ratio towards the desired target, an algorithm adjusted $D_a$, $T_m$, and $D_r$. Values were adjusted in that order in an attempt to match the desired compression ratio specified by DAKOTA. If adjustment of the three variables did not achieve

the desired compression ratio, then the design was considered unfeasible and was assigned the appropriate values, as explained above.

The injector rate shape was kept constant for all injections under all conditions. Because of the lack of available experimental data for a wide range of conditions and the fact that the nozzle's diameter is being modified, any specified injection rate shape would not be truly representative. In CONVERGE the injection duration, mass and injector nozzle diameters are specified, which results in a calculated injection pressure. Given our goal to include injection pressure as an independent variable, the relationship between fuel mass, injection duration and nozzle diameter is calculated in advance. Within this constraint, injection durations were tabulated for a range of injector nozzle diameters, fuel masses and injection pressures based on a priori calculations and used by CAESES during the optimization. EGR variations were not considered. This was a deliberate choice due to the implication that changing EGR and boost pressures would necessarily mean involving turbocharger efficiency calculations to guarantee that the conditions explored are feasible from a turbomachinery perspective. EGR is not expected to change the conclusions of this work.

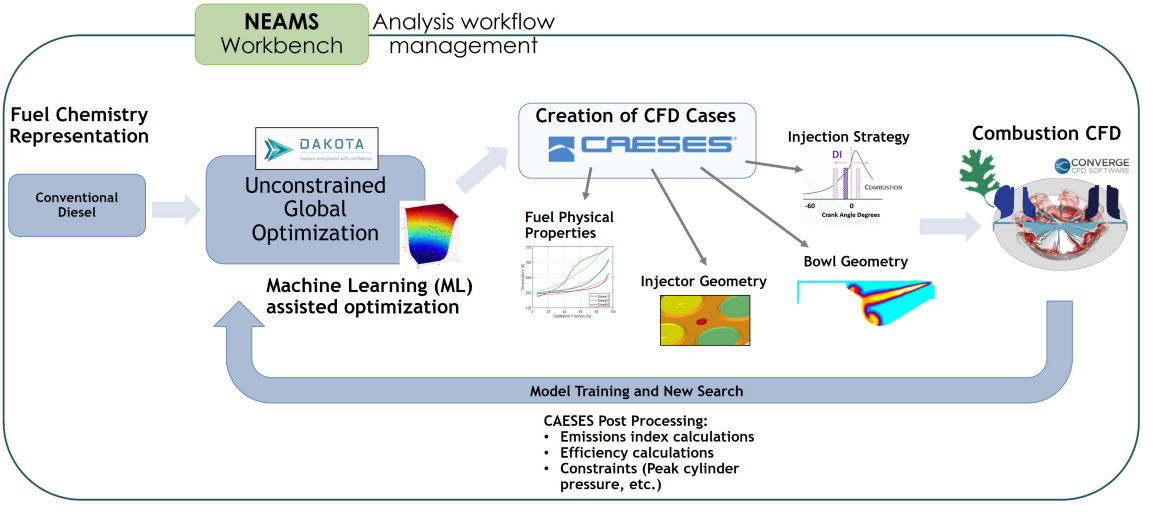


**Figure 3:** Schematic of optimization workflow used in this work.

Table 6 summarizes the ranges given to DAKOTA for each independent variable. Of the 10 independent parameters that define the piston bowl, 6 parameters were chosen as independent variables, in addition to the geometric compression ratio. As explained above, three of the variables—$D_a$, $T_m$ and $D_r$—were used as adjustment parameters for the compression ratio. The ranges were chosen after manual investigation of each parameter and their interactions. The ranges were chosen to minimize creation of unfeasible designs that would lead to inverted cell geometries and that would allow for the widest variability in piston bowl shape including, step-lipped and open-dish style bowls. This investigation found that, because of the relationship between $D_i$ and $D_b$, specifying one of the values and their difference led to fewer unfeasible designs than specifying both values independently. The variable R6 was not considered in the

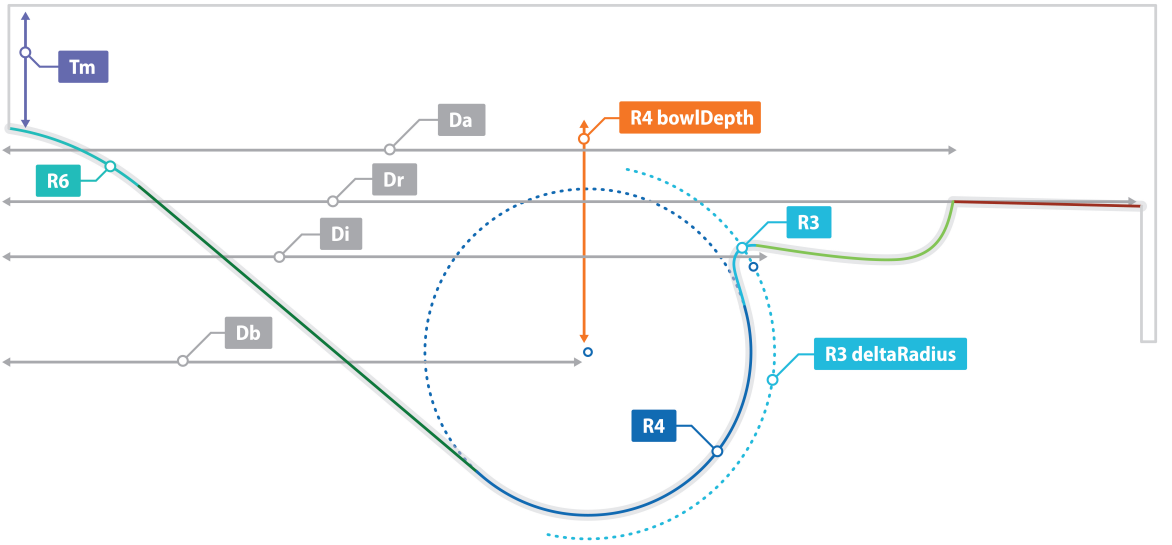


**Figure 4:** Schematic of the bowl parameterization scheme used to generate new bowl geometries.

**Table 6**
Range of variables explored in the optimization.

| | |
|---|---|
| $D_i$ - $D_b$ [mm] | -5 to 10 |
| $D_b$ [mm] | 50 to 70 |
| $r_3$ [mm] – radius | 0.75 to 2 |
| $r_3$d [mm] – delta radius | 0 to 0.5 |
| $r_4$ [mm] – radius | 4 to 8 |
| $r_4$d [mm] – bowl depth | 7.5 to 12 |
| Compression ratio (CR) [-] | 17 to 22 |
| Physical property factor [-] (density, HoV, viscosity, thermal conductivity, surface tension, $p_v$, $C_p$) | 0.8 to 1.2 |
| Rail pressure ($r_p$) [bar] | 1300 to 2000 |
| Start of post-injection [°aTDCf] | 5 to 15 |
| Post injection fraction [-] | 0.03 to 0.1 |
| Main injection fraction [-] | 0.75 to 0.90 |
| Pre-separation [°] | 5 to 15 |
| Post-separation [°] | 5 to 20 |
| Included angle [°] | 69 to 75 |
| Nozzle protrusion [m] | 0 to 0.00135 |
| Nozzle diameter [$\mu$m] | 141 to 282 |

optimization due to it not having a significant impact, and its effect being predictable, smaller values resulted in better performance for all explored cases.

Physical properties were varied at $\pm$ 20% to allow for significant changes in the results and to give the simulations the best chance of exposing any potential interaction effects between other parameters and the fuel's physical properties. All physical properties were added as independent variables for the optimization: density, heat of vaporization (HoV), viscosity, thermal conductivity, surface tension, vapor pressure ($p_v$), and heat capacity ($C_p$).

Injection strategy parameters were chosen to allow a wide variety of triple-injection strategies, including those with a large pilot-injection to allow partially premixed combustion (PPC), if so favored by the optimization. Separation between each injection was specified to prevent overlap between the injections. The spray's included angle and the nozzle's protrusion were chosen to allow for a wide variety of spray targeting. The nozzle diameter's minimum value was chosen to be the baseline, and the maximum value was chosen to be the largest nozzle diameter an 8-hole injector could realistically accommodate.

In summary, ranges for each variable were chosen to allow the widest variations and to generate the least amount of unfeasible designs.

# 3. Results and Analysis

## 3.1. Optimization Results

Figure 5 shows the results of all CFD simulations performed in this optimization. A total of 1076 functional evaluations were performed, along with a total of 612 CFD simulations. Each simulation was performed using 128 cores and took approximately 24 hours to complete. The majority of unfeasible designs was clustered in the first iterations of the optimizer, and as the GPR and EIF functions improved, unfeasible designs were largely avoided. The results show that the optimization was able to cover a wide range of conditions and was able to populate the Pareto front successfully. Results show that the typical trade-offs between NOx/GIE and NOx/Soot are fairly evident. Because of the unconstrained nature of the optimization, a higher concentration of CFD runs can be observed at higher NOx values, where the efficiency was highest. When compared with the baseline case, it can be seen that the optimization results allow an improvement in efficiency and a reduction in soot at the same or similar NOx levels. Alternatively, emissions of NOx and soot can be significantly reduced at the same efficiency levels. The maximum GIE achieved during the simulation was 45.3%, but this was at a NOx level 2.4x that of the baseline. To ensure a fair comparison between the baseline and the optimization results, a point must be chosen at a similar NOx level. Table 7 shows a comparison of inputs and outputs at an optimal condition close to NOx parity against the baseline case. A comparison of the input parameters show significant differences between the injection strategies of the two cases. The optimization case favored a lower compression ratio of 17.3 because of the large amount of fuel premixing favored by the optimization. Pilot and main injection timings were significantly advanced, with a significant amount of fuel in the pilot injection (17.5%). The spray's included angle and nozzle protrusion were adjusted to target the specific piston bowl, as shown below. Rail pressures were largely similar. However, the optimization favored the largest nozzle diameters, as expected. This led to significantly shorter injection events and improvement of the mixture preparation, which in turn enabled the improvements in GIE observed. The optimal case showed an increase in the GIE of 2.8%, with a simultaneous soot emissions reduction of 26.5% compared to the baseline at a similar NOx level.

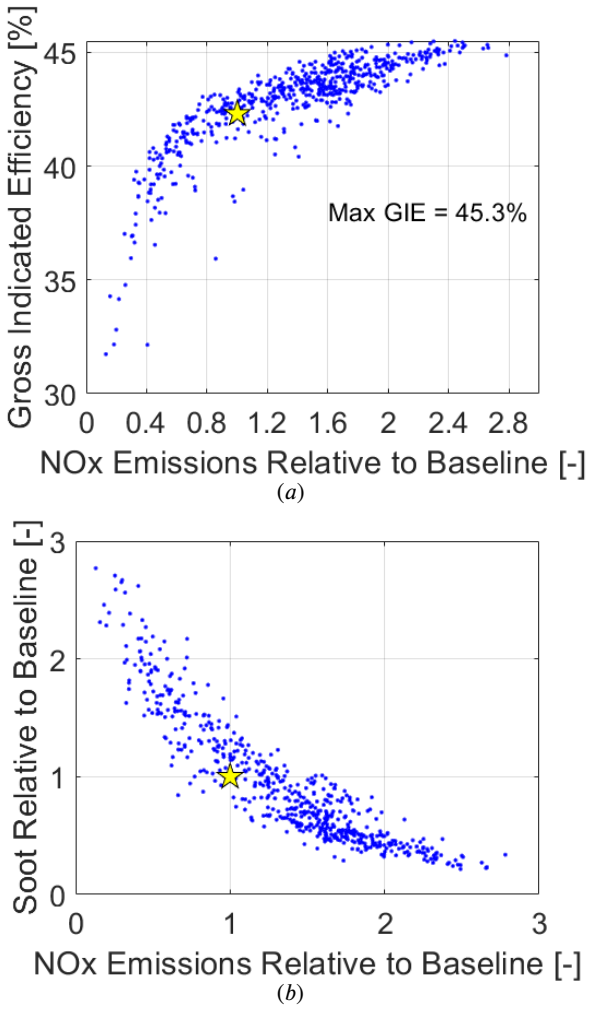


**Figure 5:** (a) Gross indicated efficiency [%] as a function of NOx emissions normalized by the baseline and (b) NOx emissions as a function of soot emissions normalized by the baseline for all 612 simulated cases. The yellow stars represent the baseline condition.

Figure 6 compares cylinder pressure and apparent heat release rate (AHRR) between the baseline case and the optimal case presented in Table 7. The AHRR results show a characteristic partially premixed combustion (PPC) regime with a large premixed spike at the start of combustion, with over 50% of the fuel burned and a long heat release tail. To achieve this, the optimization favored a lower compression ratio to reduce the compression pressure, allowing a significant portion of the fuel to be premixed while maintaining control of the ignition timing through the main injection. Nevertheless, peak cylinder pressures and peak pressure rise rates (PPRRs) were significantly higher for the optimized case. Because of the unconstrained nature of the optimization, these variables were not limited during functional evaluations. The PPRR in the optimal case was 63 bar/CA°, which is likely close to the mechanical limits of the engine. Combustion noise in dB(A) was estimated from the cylinder pressure trace, and the optimized results led to an increase of 10 dB(A). Because of the long tail of the AHRR in the optimum case, the combustion duration,

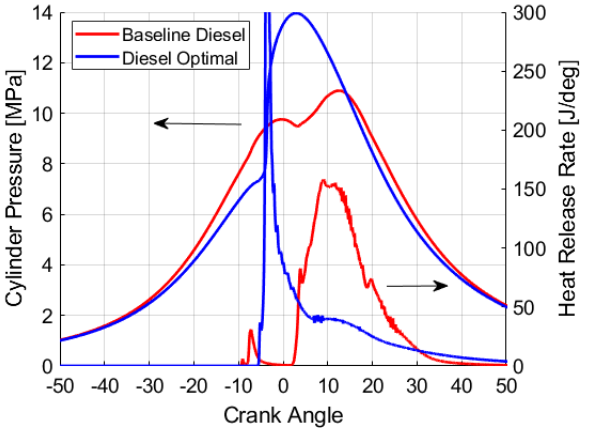


**Figure 6:** Comparison of cylinder pressure and apparent heat release rate (AHRR) between baseline diesel and diesel optimum result.

which was calculated as the crank angle distance between 10% and 90% mass fraction burned (MFB), was longer than the baseline. Table 7 shows the calculated total heat transfer and the expansion stroke utilization [35]. The results show that essentially all the efficiency gain observed was the result of a significant reduction in heat transfer for the optimum case. The longer combustion duration, which led to a lower expansion stroke utilization, along with a lower compression ratio, resulted in reductions in efficiency that were overcome by the larger reduction in heat transfer rate observed.

Figure 7 compares the piston bowl profiles between the baseline and the optimum result at TDC. The optimum bowl shape was constrained by the unique parameterization of the geometry chosen for this work. Determining the bowl shape and targeting the spray for the optimum case was fairly distinct from the diesel baseline. The baseline bowl is narrower and deeper than that of the optimum, with a lower center pip and a larger volume contained in the bottom of the bowl. The step lip in the baseline case was significantly more subtle. The spray target for the baseline case is just slightly below the protruding lip, which is typical for conventional diesel combustion systems. The lip serves to split the fuel upwards and downwards as it hits the wall. The optimum bowl had a higher center pip and an overall shallower profile. The bowl volume was split between the bottom of the bowl and the volume above the bowl lip. The squish height of the optimum case was also higher than that of the baseline. The total surface area of the bowl was reduced by 6.5% for the optimum case. Combined with the increase in TDC volume because of the lower geometric compression ratio, the surface-to-volume ratio was reduced by 19.5% and thus was at least partially responsible for the reductions in heat transfer. The spray targeting was another distinction of the optimum case. Instead of being targeted to split the fuel on the bowl lip as in a conventional diesel bowl, all of the fuel was targeted toward the bottom of the bowl, with a spray axis essentially parallel to the bowl's center slope.

**Table 7**
Comparison of baseline diesel condition and chosen optimum point.

| **Parameter** | **Optimal case** | **Baseline** |
|---|---|---|
| Compression ratio [-] | 17.3 | 20 |
| Pre-injection timing [°aTDCf] | -28.1 | -11.9 |
| Main-injection timing [°aTDCf] | -8.9 | 0.0 |
| Post-injection timing [°aTDCf] | 5.5 | 17.2 |
| Pre-injection fraction [-] | 0.175 | 0.03 |
| Main-injection fraction [-] | 0.78 | 0.85 |
| Post-injection fraction [-] | 0.045 | 0.12 |
| Rail pressure ($r_p$) [bar] | 1339 | 1500 |
| Pre-separation [°] | 19.2 | 11.9 |
| Post-separation [°] | 14.4 | 17.2 |
| Included angle [°] | 69 | 72.5 |
| Nozzle protrusion [m] | 0.0013 | 0 |
| Nozzle diameter [$\mu$m] | 274 | 141 |
| **Output** | **Optimal case** | **Baseline** |
| GIE [%] | 43.5 | 42.3 |
| NOx emissions relative to baseline [-] | 1.09 | 1.0 |
| Soot emissions relative to baseline [-] | 0.735 | 1.0 |
| CA50 [°aTDCf] | -0.3 | 12.5 |
| Combustion duration [°CA] | 30.4 | 17.9 |
| Peak cylinder pressure [bar] | 139 | 110 |
| Peak pressure rise rate [bar/°] | 63 | 4.3 |
| Estimated combustion Noise [dB(A)] | 117 | 107 |
| Heat transfer [%] | 6.0 | 8.9 |
| Expansion stroke utilization [%] | 88.1 | 90.8 |

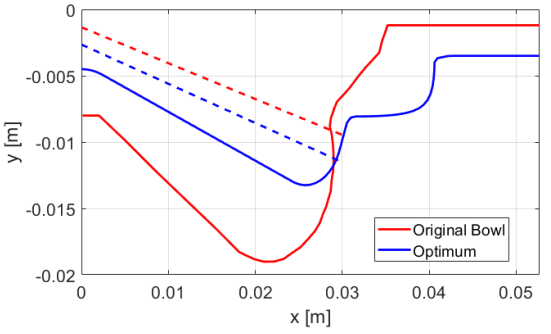


**Figure 7:** Comparison of piston bowl profiles between original baseline and optimum at TDC. Dashed lines indicate the injection spray trajectory.

The differences in bowl shape and spray targeting, along with the differences in injection strategy, resulted in significant differences in mixture preparation between cases. Figure 8a shows the distribution of fuel in certain equivalence ratio bins as a function of crank angle for the baseline and optimal cases, and it represents the bulk mixture distribution through the combustion cycle. The baseline shows a small initial bump in the equivalence ratio resulting from the pilot-injection, which is quickly consumed and mixed. The main injection event just after TDC leads to rich mixtures which persist to around 30°aTDCf. A bump in rich mixtures is seen after the post-injection event. As the main injection event progresses, the rich mixtures are continuously entrained by air, and there is a substantial increase

in lean mixtures of $0.5 < \phi < 1.0$ and $\phi < 0.5$. The optimal case shows a much larger and earlier bump in rich mixtures caused by the substantial pilot injection. The fuel quickly gets mixed into fuel lean mixtures before the main injection event. The main injection quickly creates rich mixtures which start earlier in the cycle than that seen in the baseline case, yet they persist until around the same crank angle degree. The main injection is much shorter because of the larger nozzle holes and decreased main injection fuel mass. The optimal case appears to rely on in-cylinder motion and interaction with the piston bowl to mix the fuel. Therefore, mixtures of $0.5 < \phi < 2.0$ persist for longer periods in the optimal case. In contrast, mixtures in the baseline case become over mixed more quickly.

Figure 8b shows the probability density distribution of equivalence ratio at two critical instances in time—the crank angle of 10% MFB (CA10) and CA50—which better illustrates the mixture's distribution at these points in time. The results show that at CA10, despite both cases showing a prevalence of rich mixtures, the baseline case resulted in a much broader distribution, with significantly richer fuel mixtures than seen in the optimal. At CA50, the mixture distribution for the baseline case has not changed significantly because the main injection is still occurring at CA50, and rich mixtures are still being created as a result of the air-deprived fuel jet. In the optimum case, both pilot and main injection events are completed before CA50, so there is a significant leaning of the mixtures in cylinder, with significant reductions in mixtures of $\phi > 3.0$, and a corresponding increase in mixtures of $\phi < 2.0$. Rich fuel mixtures are prevalent in both cases; consequently, it is no surprise that their NOx emissions were similar. The reduction in mixtures $\phi > 3.0$ throughout the combustion process through shorter and earlier injections is likely responsible for the decrease in soot emissions, thus improving the NOx-soot trade-off.

To gain a better understanding of the performance differences between the analyzed cases resulting from differences in the bowl shape, Figure 9 shows contour plots of the vorticity component perpendicular to the cut plane being illustrated. Neither case showed significant vorticity magnitude prior to the main injection event. The majority of the turbulence and vorticity generation was dependent upon the main injection event, as can be seen in the results. As mentioned above, the main injection targeting for the baseline case led to a split in the jet as it hit the piston walls just below the bowl lip. Vortices formed in clockwise and counter-clockwise directions as the fuel interacted with the bowl shape. The majority of the fuel was contained in the bottom of the bowl, as indicated by the black contour lines. The remainder of the fuel was pushed upwards toward the cylinder head. Strong vortices remained in the bottom of the bowl, spinning in the direction of the original spray motion, which seemed to keep the fuel mostly contained in that region. The fuel that was pushed toward the cylinder head was further pushed into the squish region by the vortices formed in that region by the step-lip geometry [11] (well observed after 10°CA). These vortices rotated in a direction opposite to the original spray motion in the region. They persisted throughout the combustion process and continued to keep the fuel contained in the main bowl volume, pushing the fuel in the squish region further toward the cylinder head and liner.

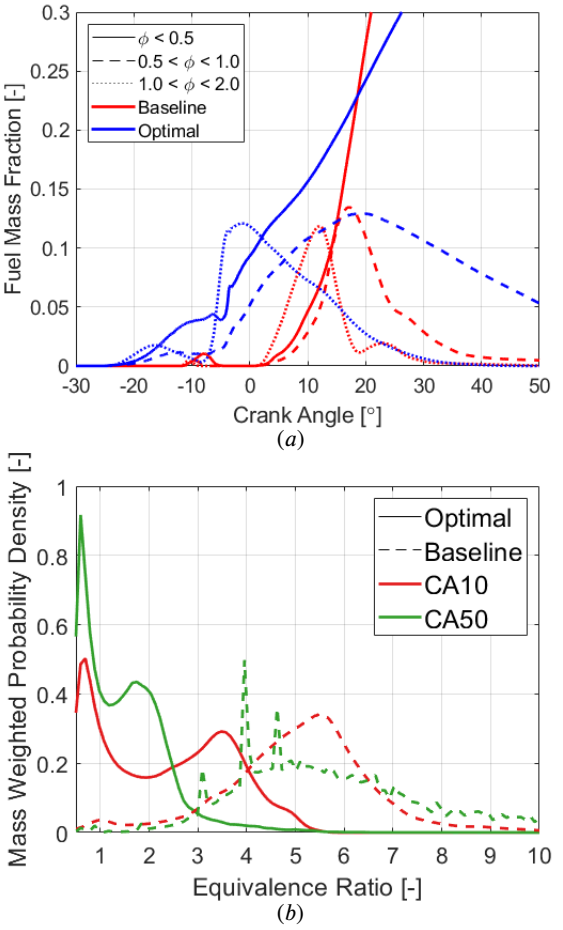


**Figure 8:** Mass fraction of fuel located inside certain equivalence ratio bins as a function of crank angle (a), and probability density distributions of equivalence ratio at CA10 and CA50 for optimal and baseline cases (b).

The optimum case showed completely different behavior. The vorticity was also introduced by the spray motion in the cylinder. The spray was targeted at the bottom of the bowl, so it was not split as in the baseline case. The fuel-rich mixtures did not stay inside the bottom of the bowl, unlike the baseline case, because the prevailing spray motion pushed the fuel out of the bottom and toward the upper lip portion. Vortices were clearly formed in the upper lip portion (observed around TDC), with orientations that kept the fuel away from the squish region (i.e., clockwise on the left portion of the contour, and counter-clockwise in the right side of the contour). The vortices maintained the fuel in the upper lip portion of the bowl in an almost toroidal shape across the entire 360° of the piston bowl. Vortices in the optimum case quickly dissipated, and fuel-rich regions remained relatively static as the combustion progressed.

The extremely high PPRR and estimated combustion noise of the optimum case have resulted in an interest to explore whether there were other potential cases in the data set with a reduced pilot-injection mass that could also deliver efficiency and emissions improvements without reaching mechanical or operational limitations. A second

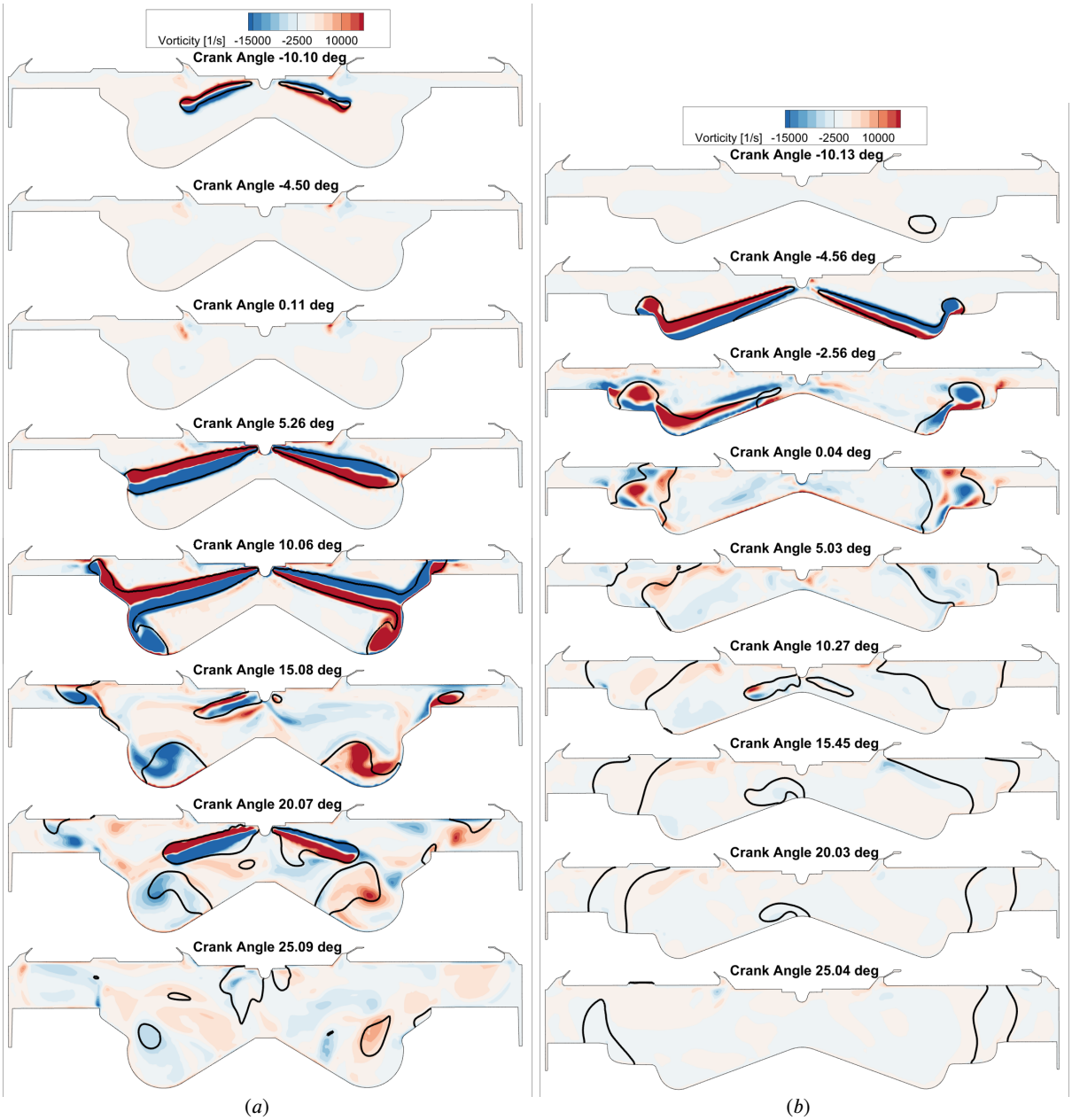


**Figure 9:** Contour plots of vorticity component perpendicular to cut section for baseline diesel (a) and optimal case (b). The black line represents the contour line of $\phi = 1.0$.

optimal case with a pilot-injection mass of 8.6% was chosen for comparison. Table 8 shows a comparison of the inputs and outputs between the baseline and the new point, and Figure 10 shows a comparison of cylinder pressure and AHRR between the cases. The bowl shape for this second optimization case is virtually indistinguishable from the first and thus will not be illustrated. The new optimal case showed improved efficiency and soot emissions for similar NOx levels like those seen in the original condition explored. However, the GIE improvement was reduced to 1.6% (vs. 2.8%), and soot improvements were reduced to 19% (vs. 26.5%). Comparison of cylinder pressure with

**Table 8**
Comparison of baseline diesel condition and optimum condition with less than 10% pre-injection fraction.

| **Parameter** | **Optimal case** | **Baseline** |
|---|---|---|
| Compression ratio [-] | 17.3 | 20 |
| Pre-injection timing [°aTDCf] | -17.5 | -11.9 |
| Main-injection timing [°aTDCf] | 0.0 | 0.0 |
| Post-injection timing [°aTDCf] | 14.4 | 17.2 |
| Pre-injection fraction [-] | 0.086 | 0.03 |
| Main-injection fraction [-] | 0.872 | 0.85 |
| Post-injection fraction [-] | 0.042 | 0.12 |
| Rail pressure ($r_p$) [bar] | 1339 | 1500 |
| Pre-separation [°] | 17.5 | 11.9 |
| Post-separation [°] | 14.4 | 17.2 |
| Included angle [°] | 74.7 | 72.5 |
| Nozzle protrusion [m] | 0.00075 | 0 |
| Nozzle diameter [$\mu$m] | 274 | 141 |
| **Output** | **Optimal case** | **Baseline** |
| GIE [%] | 43.0 | 42.3 |
| NOx emissions relative to baseline [-] | 1.08 | 1.0 |
| Soot emissions relative to baseline [-] | 0.816 | 1.0 |
| CA50 [°aTDCf] | 7.8 | 12.5 |
| Combustion duration [°CA] | 15.6 | 17.9 |
| Peak cylinder pressure [bar] | 120 | 110 |
| Peak pressure rise rate [bar/°] | 9.9 | 4.3 |
| Estimated combustion noise [dB(A)] | 106 | 107 |
| Heat transfer [%] | 9.0 | 8.9 |
| Expansion stroke utilization [%] | 93.5 | 90.8 |

heat release rates shows a much more diesel-like AHRR because of the more conventional injection strategy. A short premixed spike is observed, followed by a main heat release event after TDC. The peak heat release rate is higher than the baseline, and combustion is significantly shorter. By avoiding a high mass pilot-injection, a high PPRR was largely avoided, and the estimated combustion noise was in line with the baseline case. In contrast to the first optimal case analyzed, the GIE benefits observed were not caused by heat transfer reductions, but from improvements in the combustion thermodynamics resulting from increased rates of injection. Therefore, in this particular case, the only benefit observed was that of an increased nozzle diameter that allowed the fuel to be injected in a shorter period of time and allowed a more thermodynamically favorable heat release event. The bowl shape and compression ratio for this case were similar to those of the original optimal case, so only the injection strategy was responsible for reducing PPRR and combustion noise levels.

## 3.2. Parameter Interaction Analysis

One key question of interest in this work is to identify any potential interactions between the fuel's physical properties and other parameters of the optimization that could be leveraged in a co-optimization context. To accomplish that, a surrogate model based on Gaussian process regression (GPR) was built using all 612 CFD runs to study parametric responses on the GIE. The GPRs were built using settings similar to those used internally by DAKOTA

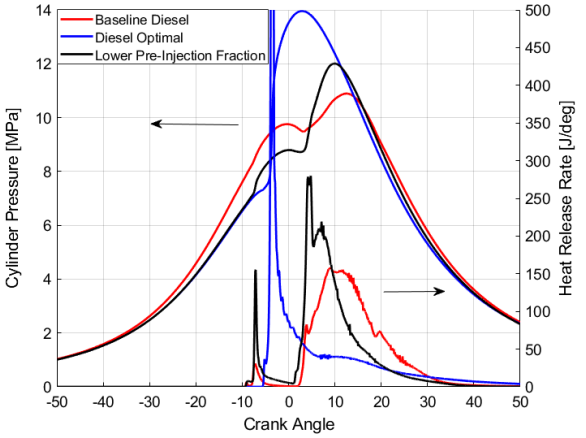


**Figure 10:** Comparison of cylinder pressure and apparent heat release rate (AHRR) between baseline diesel and optimum result.

during the optimization. The accuracy of the GPR fit is not of significant relevance to the conclusions of this section. The GPR model is simply used to find relationships between the different parameters to answer the question of whether there is an opportunity for co-optimization of fuel properties and engine geometry through parameter interactions. Nevertheless, the settings for the GPR surrogate fit were set to achieve an $R^2$ value higher than 0.9, thus the figures specific to each variable fit will not be presented for brevity. The GPR fit used an exponential kernel function with a separate length scale for each predictor and a pure quadratic basis function. Parameter optimization during the fit was performed with a Limited-memory Broyden-Fletcher-Goldfarb-Shanno algorithm. Figure 11 shows a contour of GIE as a function of pilot-injection and main injection timings as an example. The contours were created while centered around the optimal condition shown in Table 7. Therefore, while 2 variables were being varied, the others were held at the optimal value. The contours were used to create interaction plots that illustrate the potential parametric interactions. The change in GIE ($\Delta$GIE) can be calculated moving from a low value of pilot start of injection (SOI) to a high value at different levels of the main SOI. If there is a change in the $\Delta$GIE caused by spanning the pilot-injection SOI space when the main injection timing is changed, then there is a parametric interaction. That is, the main injection timing interacts with the variable in the X axis to modify its effect on the GIE. The contour clearly shows an interaction between the pilot and main injection timings. For a high value of the main SOI—that is, a delayed main injection—the pilot-injection timing has very little effect on the GIE. However, when the main injection timing is advanced, the pilot-injection timing has a significant impact on the efficiency, and higher efficiencies are observed for earlier pilot SOIs.

This analysis can be performed for all parameter combinations and illustrated in a more concise format, as shown in Figure 12, which presents the results of the analysis for fuel density and fuel heat capacity. The plot shows the change in GIE ($\Delta$GIE) in absolute numbers when varying the fuel property from +20% to −20% at a low, mid, and high value

of the remaining 22 variables, analogous to that seen visually for the contour in Figure 11. If the plot deviates from a horizontal line, then it indicates a parameter interaction. The results show that fuel density exhibited interactions with other variables. However the fuel heat capacity did not: its effect on the GIE was not changed by any other variable. The remaining fuel properties showed no interactions and will not be presented here for brevity. Fuel density showed stronger interactions with the main SOI, the nozzle diameter, the bowl depth, and the injector spray angle. This is likely the result of the strong effect that density has on the spray penetration and dynamics, and thus the mixture formation. The optimum cases relied heavily on mixture formation and fuel premixing. Therefore, in this scenario, it appears that the density can be leveraged to a certain extent to improve efficiency. In general, the results show that a decrease in density is always beneficial. This is also shown for heat capacity. However, it is important to note that the changes in GIE shown in Figure 12 are a result of a very large change in the fuel properties (±20%). In reality, these changes are not possible, so the impacts of density changes will be significantly smaller than that shown here. The results here only identify trends, whereas the magnitudes must be defined by how much these fuel properties can be changed in a real fuel.

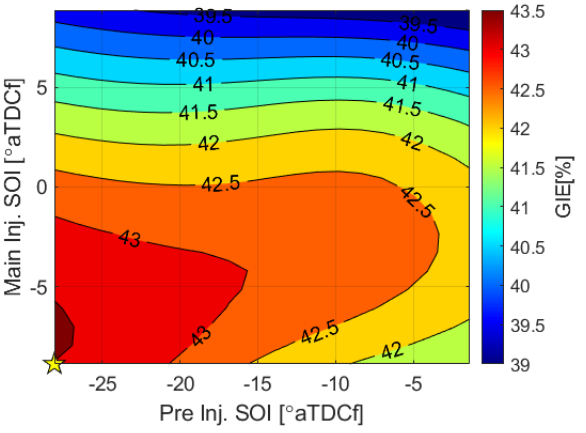


**Figure 11:** Contour plot of GIE as a function of pre- and main-injection timings for the GPR model.

Figure 13 shows the interaction plot of NOx emissions for the fuel density. The figure shows the absolute change in NOx emissions in ppm for the density change from +20% to −20%. As for GIE, other properties did not show any interaction effects for NOx and are omitted for brevity. Density interacted with almost all other 22 parameters when considering NOx emissions. The strongest interaction was observed for the injector spray angle, where a large value of the spray angle resulted in a ΔNOx of approximately 600 ppm when varying the fuel density, whereas for a narrower spray angle, the ΔNOx was only approximately 100 ppm. This is similar to the interaction effect of density with spray angle for GIE. Spray targeting seems to have a significant influence on the total effect of fuel density change. A similar analysis was conducted for soot emissions, but no interaction effects were found between physical properties and soot.

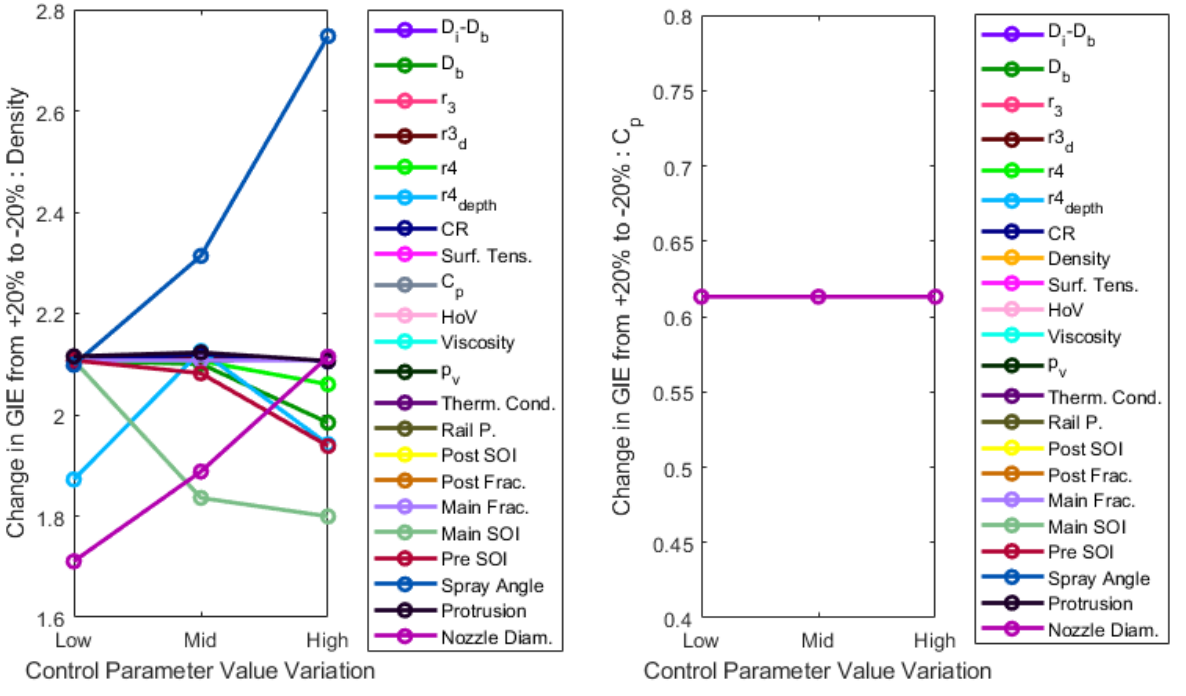


(*a*) (*b*)

**Figure 12:** Interaction plot of GIE for fuel density (a) and heat capacity ($C_p$) (b).

The analysis thus far was conducted assuming the optimal point in Table 7 as the center point for variations in each independent variable. Therefore, the interaction effects observed can be solely associated with the characteristics of the PPC regime, where mixture preparation prior to ignition is critical for performance. Figure 14 shows the analysis performed with the diffusion-limited diesel-like optimum shown in Table 8 as the center for variations. The results show that density had interactions with variables that influence mixture formation, as in the main injection timing, nozzle diameter and protrusion, and spray angle. However, the magnitude of the interaction effects was reduced. Similarly, interaction effects were seen for all variables, as shown in Figure 14b, but all interactions effects were small, with maximum changes in ΔNOx of approximately 50 ppm. In conclusion, it appears that the mixing-limited combustion regime showed weaker interaction effects with fuel physical properties, likely because of the relative insensitivity of the combustion performance to mixture preparation effects.

Give that physical properties were allowed to change during the optimization it is important to quantify what their contribution was to the final efficiency numbers. The GPR model generated to study interaction effects can be used to isolate physical property effects. Table 9 shows a comparison of GIE between the baseline case, the optimum diesel case in the PPC regime and the low-pre-injection fraction mixing-limited diesel optimum case with and without changes to fuel physical properties. The results show that most of the improvement in efficiency observed for both optimum cases

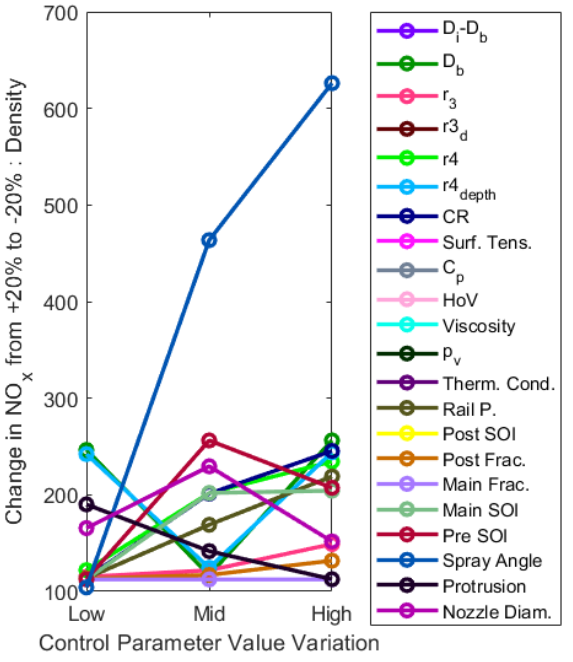


**Figure 13:** Interaction plot of NOx for fuel density.

.

**Table 9**
Comparison of GIE for baseline, and the two optimum conventional diesel cases with and without physical property changes to the fuel

| | Baseline | Optimum | Low-Pre-Injection Optimum |
|---|---|---|---|
| GIE [%] | 42.3 | 43.5 | 43 |
| GIE without fuel physical property changes [%] | N/A | 42.7 | 42.3 |

were caused by the changes in physical properties. Previous discussion showed some interaction between density in particular and other control parameters associated with mixture formation. Therefore, it is not surprising that substantial changes in density and other physical properties could contribute up to 0.8% absolute points in engine efficiency. Nevertheless, the trends of increased fuel rate of injection should still provide some efficiency benefits over the baseline case.

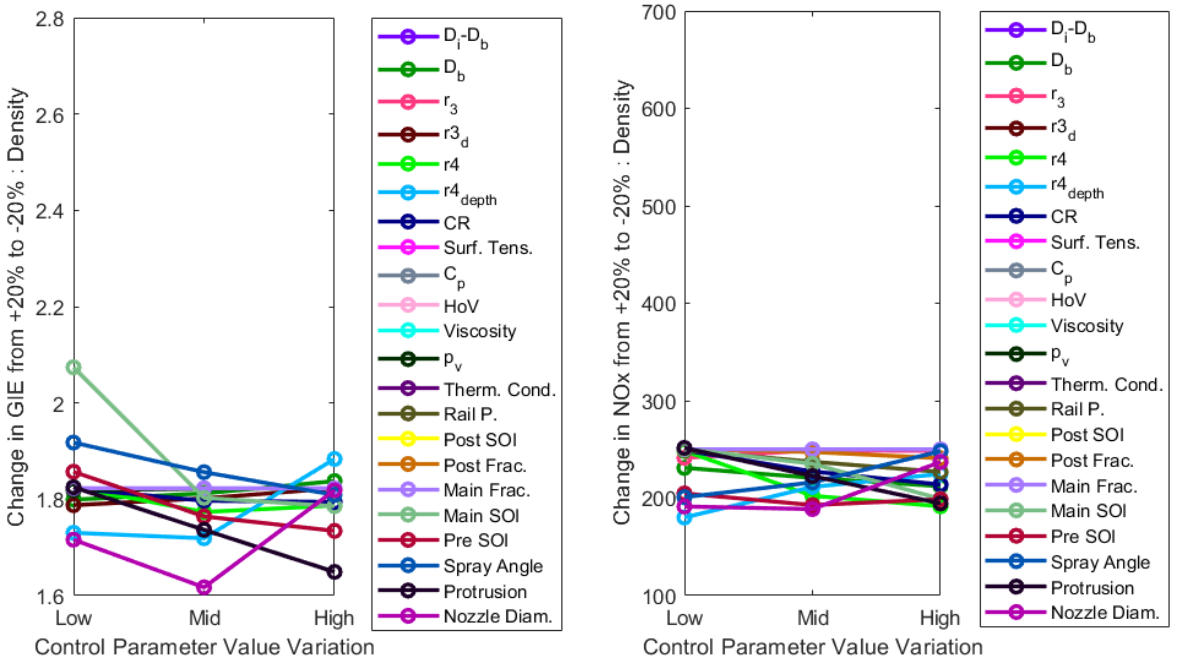


(*a*) (*b*)

**Figure 14:** Interaction plot for fuel density of GIE (a) and NOx (b) centered around the optimal point in Table 8.

## 4. Conclusions

Computational fluid dynamics simulations, coupled with an advanced machine learning–assisted global optimizer, was used to explore a wide design space for a total of 23 independent variables. For the first time, physical property variations were included as independent variables in the optimization. Through detailed analysis of the results, the following conclusions can be drawn:

- The unconstrained global optimization was able to improve on the baseline diesel case, with improved emissions and efficiency trade-offs. The optimal case chosen for comparison leveraged a PPC regime with a large pilot injection and resulted in an improvement in GIE of 2.8% with a simultaneous 26.5% reduction in soot at a similar NOx level. The vast majority of efficiency benefits came in the form of reduced heat transfer losses, which were a result of the improved surface-to-volume ratio of the combustion chamber and different in-cylinder flame dynamics. Avoidance of extremely fuel-rich zones during the combustion process were responsible for soot reductions. Because of the unconstrained nature of the optimization, the PPRR and the estimated combustion noise were excessively high. Further analysis of the response surface showed that without fuel physical property changes efficiency improvements were limited to a 0.9% increase.

- Because of the high PPRR and combustion noise of the optimum PPC case, a second optimum case targeting a mixing-limited combustion regime was chosen for comparison. The case showed that, even while avoiding the PPC regime, improvements in efficiency and soot are possible at similar NOx levels. Nevertheless, GIE improvement was reduced to 1.6%, and soot was reduced to 19%. In this case, GIE improvements were associated solely with a faster burn rate, a result of larger injector nozzle sizes. Consequently, it can be concluded that nozzle diameter and faster injection rates are the strongest lever to increase mixing-limited combustion performance when compared to the baseline. Nevertheless, like the results for the PPC regime, efficiency benefits seem to be mostly tied to modifications of the fuel's physical properties. When fuel physical property effects are removed, the second optimum cases did not offer any efficiency benefits over the baseline.

- The piston bowl in the optimum cases did not behave as in the baseline. Vortex structures formed in the cylinder as a result of the turbulence induced by the fuel spray. These structures were very distinct and resulted in spatial and temporal differences in fuel and temperature distributions.

- Interaction effects between physical properties and other variables are minimal for realistic changes in fuel property values. Except for fuel density, no interactions were observed between physical properties and other variables that could be leveraged in a co-optimization context. Stronger interaction effects between density and other variables were observed in the PPC regime associated with its higher sensitivity to mixture

preparation prior to ignition. However, these interaction effects became even smaller when considering a mixing-limited combustion regime in which there is a relative insensitivity of the combustion performance to mixture preparation effects. Therefore, physical properties cannot be leveraged in a co-optimization context, so the fuel's physical properties can be adjusted in isolation for best performance. Nevertheless, a large percentage of the efficiency gains observed in the simulations stemmed from changes in fuel physical properties. However, the changes proposed by the model can not be realized in a practical fuel. Other changes proposed by the model such as increased injection rates should still provide benefits over the baseline condition.

## 5. Acknowledgements

The authors would like to acknowledge funding from the US DOE Office of Energy Efficiency and Renewable Energy, with special thanks to program manager Kevin Stork. This research used resources of the Compute Data Environment for Science (CADES) at Oak Ridge National Laboratory, which is supported by the Office of Science of the US Department of Energy under Contract no. DE-AC05-00OR22725. The authors would like to thank Convergent Science for providing licenses to Converge, which enabled this work. Authors would like to thank Russell Whitesides for development of fuel surrogates for this project.

## Nomenclature

| | |
|---|---|
| $\phi$ | fuel–air equivalence ratio |
| °CA | crank angle degrees |
| $NO_x$ | nitrogen oxides |
| AHRR | apparent heat release rate |
| aTDCf | after top dead center of firing |
| BDC | bottom dead center |
| CA10 | crank angle at 10% of total heat release (combustion phasing) |
| CA50 | crank angle at 50% of total heat release (combustion phasing) |
| CAD | computer-aided design |
| CARB | California Air Resources Board |
| CFD | computational fluid dynamics |
| CO | carbon monoxide |
| CR | compression ratio |
| $D_b$ | width to $r_4$ center |
| $D_i$ | width to $r_3$ center |
| DI | direct injection |

EGR exhaust gas recirculation

GIE gross indicated efficiency

GPR Gaussian process regression

HC hydrocarbons

HPC high-performance computing

IMEP indicated mean effective pressure

KH-RT Kelvin-Helmholtz Rayleigh-Taylor

LHV lower heating value

MCCI mixing controlled compression ignition

NEAMS nuclear energy advanced modeling and simulation

NTC no time counter

ORNL Oak Ridge National Laboratory

PDF probability density function

PPC partially premixed combustion

$r_3$ lip radius

$r_3d$ distance between lip center and bowl circle

$r_4$ bowl circle radius

$r_4d$ bowl depth

RANS Reynolds-averaged Navier–Stokes

SOI start of injection

TDC top dead center

TKE turbulent kinetic energy

TWC three-way catalyst

# References


[1] M. A. Groendyk, D. Rothamer, Effects of fuel physical properties on auto-ignition characteristics in a heavy duty compression ignition engine, SAE International Journal of Fuels and Lubricants 8 (2015) 200–213. URL: https://doi.org/10.4271/2015-01-0952. doi:https://doi.org/10.4271/2015-01-0952.

[2] F. D.F. Chuahy, S. L. Kokjohn, Effects of the direct-injected fuel's physical and chemical properties on dual-fuel combustion, Fuel 207 (2017) 729–740. URL: https://www.sciencedirect.com/science/article/pii/S0016236117307391. doi:https://doi.org/10.1016/j.fuel.2017.06.039.

[3] Y. Ra, R. D. Reitz, J. McFarlane, C. S. Daw, Effects of fuel physical properties on diesel engine combustion using diesel and bio-diesel fuels, SAE International Journal of Fuels and Lubricants 1 (2008) 703–718. URL: https://doi.org/10.4271/2008-01-1379. doi:https://doi.org/10.4271/2008-01-1379.

[4] Y. Zhang, A. Voice, Y. Pei, M. Traver, D. Cleary, A Computational Investigation of Fuel Chemical and Physical Properties Effects on Gasoline Compression Ignition in a Heavy-Duty Diesel Engine, Journal of Energy Resources Technology 140 (2018) 102202. doi:10.1115/1.4040010.

[5] H. Liu, Z. Zheng, M. Yao, Effects of fuel physical and chemical properties on combustion and emissions on both metal and optical diesel engines and on a partially premixed burner, in: JSAE/SAE 2015 International Powertrains, Fuels Lubricants Meeting, SAE International, 2015. URL: https://doi.org/10.4271/2015-01-1918. doi:https://doi.org/10.4271/2015-01-1918.

[6] F. D. F. Chuahy, C. S. Sluder, S. J. Curran, G. Kukkadapu, S. W. Wagnon, R. Whitesides, Numerical assessment of fuel physical properties on high-dilution diesel advanced compression ignition combustion, Applications in Energy and Combustion Science 13 (2023) 100102. URL: https://www.sciencedirect.com/science/article/pii/S2666352X22000450. doi:https://doi.org/10.1016/j.jaecs.2022.100102.

[7] F. D. F. Chuahy, Multi-injection investigation of a high-volatility diesel in advanced compression ignition combustion for NOx control, International Journal of Engine Research 24 (2023) 3850–3862. URL: https://doi.org/10.1177/14680874231180361. doi:10.1177/14680874231180361. arXiv:https://doi.org/10.1177/14680874231180361.

[8] Y. İçıngür, D. Altiparmak, Effect of fuel cetane number and injection pressure on a di diesel engine performance and emissions, Energy Conversion and Management 44 (2003) 389–397. URL: https://www.sciencedirect.com/science/article/pii/S0196890402000638. doi:https://doi.org/10.1016/S0196-8904(02)00063-8.

[9] T. L. Ullman, R. L. Mason, D. A. Montalvo, Effects of fuel aromatics, cetane number, and cetane improver on emissions from a 1991 prototype heavy-duty diesel engine, in: International Fuels Lubricants Meeting Exposition, SAE International, 1990. URL: https://doi.org/10.4271/902171. doi:https://doi.org/10.4271/902171.

[10] H. Yuan, T. Tsukuda, Y. Yang, G. Shibata, Y. Kobashi, H. Ogawa, Effects of chemical compositions and cetane number of fischer–tropsch fuels on diesel engine performance, Energies 15 (2022). URL: https://www.mdpi.com/1996-1073/15/11/4047. doi:10.3390/en15114047.

[11] S. Busch, F. Perini, R. Reitz, E. Kurtz, Effects of stepped-lip combustion system design and operating parameters on turbulent flow evolution in a diesel engine, SAE International Journal of Engines 13 (2020) 223–240. URL: https://doi.org/10.4271/03-13-02-0016. doi:https://doi.org/10.4271/03-13-02-0016.

[12] D. D. Wickman, P. K. Senecal, R. D. Reitz, Diesel engine combustion chamber geometry optimization using genetic algorithms and multi-dimensional spray and combustion modeling, in: SAE 2001 World Congress, SAE International, 2001. URL: https://doi.org/10.4271/2001-01-0547. doi:https://doi.org/10.4271/2001-01-0547.

[13] N. K. Mukherjee, S. Rapol, S. Unnithan, D. Nene, Optimization of a 3D combustion bowl geometry using response surface modeling, SAE International Journal of Engines 14 (2020) 173–198. URL: https://doi.org/10.4271/03-14-02-0011. doi:https://doi.org/10.4271/03-14-02-0011.

[14] J. Benajes, R. Novella, J. M. Pastor, A. Hernández-López, M. Hasegawa, N. Tsuji, M. Emi, I. Uehara, J. Martorell, M. Alonso, Optimization of the combustion system of a medium duty direct injection diesel engine by combining CFD modeling with experimental validation, Energy Conversion and Management 110 (2016) 212–229. URL: https://www.sciencedirect.com/science/article/pii/S0196890415010985. doi:https://doi.org/10.1016/j.enconman.2015.12.010.

[15] Y. Shi, R. D. Reitz, Optimization study of the effects of bowl geometry, spray targeting, and swirl ratio for a heavy-duty diesel engine operated at low and high load, International Journal of Engine Research 9 (2008) 325–346. URL: https://doi.org/10.1243/14680874JER00808. doi:10.1243/14680874JER00808. arXiv:https://doi.org/10.1243/14680874JER00808.

[16] R. Şener, M. Z. Gül, Optimization of the combustion chamber geometry and injection parameters on a light-duty diesel engine for emission minimization using multi-objective genetic algorithm, Fuel 304 (2021) 121379. URL: https://www.sciencedirect.com/science/article/pii/S0016236121012588. doi:https://doi.org/10.1016/j.fuel.2021.121379.

[17] F. Perini, K. Zha, S. Busch, E. Kurtz, R. C. Peterson, A. Warey, R. D. Reitz, Piston geometry effects in a light-duty, swirl-supported diesel engine: Flow structure characterization, International Journal of Engine Research 19 (2018) 1079–1098. URL: https://doi.org/10.1177/1468087417742572. doi:10.1177/1468087417742572. arXiv:https://doi.org/10.1177/1468087417742572.

[18] Y. Pei, P. Pal, Y. Zhang, M. Traver, D. Cleary, C. Futterer, M. Brenner, D. Probst, S. Som, CFD-guided combustion system optimization of a gasoline range fuel in a heavy-duty compression ignition engine using automatic piston geometry generation and a supercomputer, SAE International Journal of Advances and Current Practices in Mobility 1 (2019) 166–179. URL: https://doi.org/10.4271/2019-01-0001. doi:https://doi.org/10.4271/2019-01-0001.

[19] S. Subramanian, B. Rathinam, J. I. J. Lalvani, K. Annamalai, Piston bowl optimization for single cylinder diesel engine using CFD, in: International Mobility Conference, SAE International, 2016. URL: https://doi.org/10.4271/2016-28-0107. doi:https://doi.org/10.4271/2016-28-0107.

[20] B. Adams, W. Bohnhoff, K. Dalbey, M. Ebeida, J. Eddy, M. Eldred, R. Hooper, P. Hough, K. Hu, J. Jakeman, M. Khalil, K. Maupin, J. Monschke, E. Ridgway, A. Rushdi, D. Seidl, J. Stephens, L. Swiler, , J. Winokur, Dakota, A Multilevel Parallel Object-Oriented Framework for Design Optimization, Parameter Estimation, Uncertainty Quantification, and Sensitivity Analysis: Version 6.15 User's Manual, Technical Report, Sandia Technical Report, 2021.

[21] J. C. Beale, R. D. Reitz, Modeling spray atomization with the Kelvin-Helmholtz/Rayleigh-Taylor hybrid model, Atomization and Sprays 9 (1999) 623–650.

[22] D. P. Schmidt, C. Rutland, A new droplet collision algorithm, Journal of Computational Physics 164 (2000) 62–80. URL: https://www.sciencedirect.com/science/article/pii/S0021999100965689. doi:https://doi.org/10.1006/jcph.2000.6568.

[23] P. J. O'Rourke, A. A. Amsden, The tab method for numerical calculation of spray droplet breakup, in: 1987 SAE International Fall Fuels and Lubricants Meeting and Exhibition, SAE International, 1987. URL: https://doi.org/10.4271/872089. doi:https://doi.org/10.4271/872089.

[24] Amsden A.A, O'Rourke, P.J, Butler, T.D., Kiva–ii: A computer program for chemically reactive flows with sprays (1989).

[25] F. D. F. Chuahy, Multi-injection investigation of a high-volatility diesel in advanced compression ignition combustion for nox control, International Journal of Engine Research 24 (2023) 3850–3862. URL: https://doi.org/10.1177/14680874231180361. doi:10.1177/14680874231180361. arXiv:https://doi.org/10.1177/14680874231180361.

[26] F. DFChuahy, C. S. Sluder, S. J. Curran, G. Kukkadapu, S. W. Wagnon, R. Whitesides, Numerical assessment of fuel physical properties on high-dilution diesel advanced compression ignition combustion, Applications in Energy and Combustion Science 13 (2023) 100102. URL: https://www.sciencedirect.com/science/article/pii/S2666352X22000450. doi:https://doi.org/10.1016/j.jaecs.2022.100102.

[27] H. Hiroyasu, T. Kadota, Models for combustion and formation of nitric oxide and soot in direct injection diesel engines. (1976).

[28] A. B. Dempsey, P. Seiler, K. Svensson, Y. Qi, A comprehensive evaluation of diesel engine CFD modeling predictions using a semi-empirical soot model over a broad range of combustion systems, SAE International Journal of Engines 11 (2018) 1399–1420. URL: https://doi.org/10.4271/2018-01-0242. doi:https://doi.org/10.4271/2018-01-0242.

[29] F. D.F. Chuahy, S. L. Kokjohn, High efficiency dual-fuel combustion through thermochemical recovery and diesel reforming, Applied Energy 195 (2017) 503–522. URL: https://www.sciencedirect.com/science/article/pii/S0306261917302933. doi:https://doi.org/10.1016/j.apenergy.2017.03.078.

[30] R. A. Lefebvre, B. R. Langley, L. P. Miller, M.-O. G. Delchini, M. Baird, J. P. Lefebvre, NEAMS workbench status and capabilities (2019). URL: https://www.osti.gov/biblio/1570117. doi:10.2172/1570117.

[31] M.-O. G. Delchini, L. P. Swiler, R. A. Lefebvre, Extension of the neams workbench to parallel sensitivity and uncertainty analysis of thermal hydraulic parameters using dakota and nek5000, Nuclear Engineering and Technology 53 (2021) 3449–3459. URL: https://www.sciencedirect.com/science/article/pii/S1738573321001807. doi:https://doi.org/10.1016/j.net.2021.04.005.

[32] C. Kavuri, S. L. Kokjohn, Exploring the potential of machine learning in reducing the computational time/expense and improving the reliability of engine optimization studies, International Journal of Engine Research 21 (2020) 1251–1270. URL: https://doi.org/10.1177/1468087418808949. doi:10.1177/1468087418808949. arXiv:https://doi.org/10.1177/1468087418808949.

[33] D. Ginsbourger, R. Le Riche, L. Carraro, A Multi-points Criterion for Deterministic Parallel Global Optimization based on Gaussian Processes, Technical Report, 2008. URL: https://hal.science/hal-00260579.

[34] D. Ginsbourger, R. Le Riche, L. Carraro, Kriging Is Well-Suited to Parallelize Optimization, Springer Berlin Heidelberg, Berlin, Heidelberg, 2010, pp. 131–162. URL: https://doi.org/10.1007/978-3-642-10701-6_6. doi:10.1007/978-3-642-10701-6_6.

[35] W. F. Northrop, W. Fang, B. Huang, Combustion Phasing Effect on Cycle Efficiency of a Diesel Engine Using Advanced Gasoline Fumigation, Journal of Engineering for Gas Turbines and Power 135 (2013) 032801. doi:10.1115/1.4007757.